Research Article

Nano Research
2022, 15(4): 3204–3212

ISSN 1998-0124 CN 11-5974/O4
https://doi.org/10.1007/s12274-021-3938-2

The highly dispersed Co-based nanoparticles encapsulated into porous N-doping carbon polyhedral with the low content of Ru modification as a promising cathode catalyst for long-life Li-O_2 batteries

Yiru Ma[1], Huiqi Qu[4], Zhenzhen Chi[1], Xiaoqiang Liu[1], Yueqin Yu[2], Ziyang Guo[1] (✉), and Lei Wang[1,3] (✉)

[1] *Key Laboratory of Eco-chemical Engineering, Taishan Scholar Advantage and Characteristic Discipline Team of Eco-chemical Process and Technology, College of Chemistry and Molecular Engineering, Qingdao University of Science and Technology, Qingdao 266042, China*
[2] *College of Chemistry and Molecular Engineering, Qingdao University of Science and Technology, Qingdao 266042, China*
[3] *College of Environment and Safety Engineering, Qingdao University of Science and Technology, Qingdao 266042, China*
[4] *Key Laboratory of Eco-chemical Engineering, Taishan Scholar Advantage and Characteristic Discipline Team of Eco-chemical Process and Technology, College of Chemical Engineering, Qingdao University of Science and Technology, Qingdao 266042, China*

Received: 2 July 2021 / **Revised:** 30 August 2021 / **Accepted:** 15 October 2021

ABSTRACT

Lithium (Li)-O_2 batteries have triggered worldwide interest due to their ultrahigh theoretical energy density. However, it is a long shot for the grand-scale applications of Li-O_2 battery at current stage owing to its significant polarization, inferior cycling life, and irreversible decomposition of Li_2O_2. Herein, a facile way of preparing the highly dispersed Co-based nanoparticles encapsulated into porous N-doping carbon polyhedral with the low content of Ru modification (LRu@HDCo-NC) is explored through the pyrolysis of Co/Zn based zeolitic imidazole frameworks (ZIFs) containing Ru-based ligands. Even with the very small amount of Ru introduction (1.8%), LRu@HDCo-NC still exhibits the superior oxygen evolution reaction/oxygen reduction reaction (OER/ORR) performance and also inhibits side reactions in Li-O_2 battery because of the abundant pores, plentiful surface N heteroatoms, and highly dispersed metal-based sites which are induced by the volatilization of Zn, and conductive/stable carbon skeleton derived from ZIFs. When applied in Li-O_2 batteries, LRu@HDCo-NC cathode delivers a high discharge capacity of 15,973 mAh·g^{-1} at 200 mA·g^{-1}, good capacity retention at higher rate (12,362 mAh·g^{-1} at 500 mA·g^{-1}) and outstanding stability for > 300 cycles with low voltage polarization of < 2.3 V under a cut-off capacity of 1,000 mAh·g^{-1} at 500 mA·g^{-1}. More critically, a series of *ex situ* and *in situ* characterization technologies disclose that the LRu@HDCo-NC cathodes can effectively promote the reversible reactions in Li-O_2 batteries.

KEYWORDS

zeolitic imidazole frameworks, Zn volatilization, high dispersed Co-based particles, Ru modification, rechargeable Li-O_2 batteries

1 Introduction

To meet human's ever-growing demands for long-range electromobiles, a great deal of research effort has been devoted to radically exploring the new high-energy-density battery systems [1–3]. Li-O_2 batteries have been the subject of much focus owing to their incomparably high theoretical energy density [4–6]. A typical rechargeable Li-O_2 battery is generally made up of a Li anode, a Li-containing electrolyte, and a catalytic cathode, which is based on the reversible reaction between metallic Li and O_2 [7, 8]. Upon discharge, O_2 reacts with Li ion on the cathode through oxygen reduction reaction (ORR) to form Li_2O_2 and generate electricity [9–11]. During recharge process, Li_2O_2 decomposes and O_2 is released by the oxygen evolution reaction (OER), thereby storing energy [12–14]. Although this novel Li-O_2 system has received a lot of scientific interests, there are still many challenges to be solved before its practical application [15, 16], mainly including the sluggish kinetics over the ORR/OER process, the complex intermediate reactions, and the accumulation of the insulating/insoluble discharge products, which usually lead to the large polarization, poor rate capability, and inferior cycling life [17–24]. Hence, developing the high-efficient and porous catalyst is needed urgently for the high-performance Li-O_2 batteries [25–28].

Transition-metals (TMs) or their derivatives (e.g., nitrides, phosphides, oxides, and sulfides) based carbon composites recently have been investigated as the cathode catalysts in the Li-O_2 cells due to good catalytic activities [29, 30]. For example, Yu et al. have prepared hierarchical N-doped graphene cross-linked uniform cobalt oxide nanoparticles and further used the nanoparticles as the cathode to construct the Li-O_2 cell which delivered a superior capacity and comparable cycling life [31]. Among these TM-based composites, metal-organic frameworks (MOFs)-derived materials are considered as one of the most

Address correspondence to Ziyang Guo, zyguo@qust.edu.cn; Lei Wang, inorchemwl@126.com

promising catalysts for the Li-O_2 batteries because of their high surface area, abudant pores, plentiful active sites, typical mosaic structure, and stable carbon framework [32–34]. For example, Wang's group [34] has synthesized the Co nanoparticles-based catalyst with three-dimentional (3D)-print self-standing architecture derived from Co-based zeolitic imidazolate frameworks (ZIFs) which displays the high discharge capacity in the Li-O_2 batteries. Unfortunately, there are serious agglomerations for the TM-based active sites in MOFs derivatives during the calcining process, which negatively affects the performance of the Li-O_2 cells. To target this issue, many recent works have attempted to introduce the additional TMs into MOFs which can realize the highly dispersed TM-based active sites in the derivates. For instance, Chen's group [35] applied the bimetallic Fe/Co-MOF as the precursor to prepare micro-meso-macroporous FeCo-N-C-X, which improves the rate capability and cycle stability of Li-O_2 cell due to the higly dispersed FeCo-based sites. However, the TM-based composites often show the low catalytic activity in the organic electrolytes, which leads to the relatively high overpotential of the corresponding Li-O_2 batteries. Nowadays, the noble metal-based catalysts, especially ruthenium (Ru) or iridium (Ir)-based materials, exhibit the excellent ORR/OER performance and also inhibit the side reactions in Li-O_2 cells, which effectively reduce the overpotentials and improve battery reversibility [36]. It is well known that the high cost and scarcity of precious metals limit their further application in energy storage systems. Many researchers started to reduce the loading mass of noble metals in the catalysts through the ultra-small particle size of precious metals or their extra-high atom utilization. Xu et al. have synthesized the Ru single atoms distributed in porous nitrogen-doped carbon (Ru SAs-NC), which obviously decreases the discharge overpotential and regulates the morphology of discharge product [37]. However, the content of Ru in the optimized Ru SAs-NC catalyst is still not very low and the corresponding enhanced performance is also not very satisfactory. Therefore, the bi-metallic MOFs derivatives with low content of noble-metal modification should be the ideal cathode for the high-performance Li-O_2 batteries.

Herein, we firstly synthesized the Co, Zn dual-metal ZIFs (Co/Zn-ZIFs) through the seed-mediated strategy and then used these porous Co/Zn-ZIFs to absorb the Ru-containing ligands. The obtained composite was further treated with the high-temperature pyrolysis to form the highly dispersed Co-based nanoparticles encapsulated into porous N-doping carbon polyhedral with the low content of Ru modification (LRu@HDCo-NC), which is further used as the catalyst in Li-O_2 batteries. The carbon skeleton realizes the highly conductivity and electrochemical stablity of LRu@HDCo-NC. In addition, the emission of Zn vapor not only generates the large number of pores in the carbon-based framework which are beneficial for the conversion of Li_2O_2/O_2, but also optimizes the surface content of the N-based active phases which can effectively enhance the ORR performance of LRu@HDCo-NC. Moreover, the highly dispersed Ru/Co-based nanoparticles can significantly improve the catalytic activity of LRu@HDCo-NC towards OER and inhibit the side reactions in Li-O_2 batteries. As a result, the Li-O_2 battery with LRu@HDCo-NC electrode exhibits good performance, including high reversible capacity, low overpotential, and long-life cycling stability.

2 Experimental

2.1 LRu@HDCo-NC and its precursor $Ru(acac)_3$ modified Co/Zn-ZIFs ($Ru(acac)_3$@Co/Zn-ZIFs) preparation

For the preparation of $Ru(acac)_3$@Co/Zn-ZIFs, 0.616 g (7.50 mmol) 2-methylimidazole was firstly dissolved in 15 mL of methanol to obtain a clear solution (donated as solution A). Additionally, 0.073 g (0.25 mmol) of $Co(NO_3)_2{\cdot}6H_2O$, 0.558 g (0.5 mmol) $Zn(NO_3)_2{\cdot}6H_2O$, and 0.0996 g $Ru(acac)_3$ (0.25 mmol) were added to 16 mL methanol to form solution B. Afterwards, solution B was quickly added in the above solution A with vigorous stirring. The mixed solution was ultrasonized for 15 min and then transferred into the constant temperature of 35 °C water bath for 12 h. The sediment was obtained by centrifugation and following washing with methanol for several times. Then, the $Ru(acac)_3$@Co/Zn-ZIFs sediment was further dried at 60 °C in the vacuum oven. Subsequently, the obtained $Ru(acac)_3$@Co/Zn-ZIFs powder was heated to 900 °C at a rate of 5 °C·min^{-1} and further calcined at 900 °C for 3 h under the N_2 atmosphere. Upon naturally cooling down, the LRu@HDCo-NC was finally synthesized. Additionally, the porous N-doping carbon polyhedra with low content of Ru (named as LRu@NC) and N-doping carbon polyhedra (named as NC) were also prepared with the similar method (their corresponding preparations were given in the Electronic Supplementary Material (ESM)).

2.2 Li-O_2 batteries fabrication and electrochemical measurements

All the batteries assembly was operated in a glove box filled with pure argon (O_2 < 0.1 ppm and H_2O < 0.1 ppm). The detailed construction process was as follows: Firstly, the as-prepared LRu@HDCo-NC composite based electrode (the preparation of the cathodes was given in the ESM) was used as air cathode and Li foil was used as anode, respectively. Then, the celgard membrane dipped with 1 M tetraethylene glycol dimethyl ether (TEGDME)/bis (trifluoromethane) sulfonamide lithium salt (LiTFSI) was used to separate the LRu@HDCo-NC cathode and Li anode. In addition, there was a hole with the area of ~ 0.8 cm^2 on the cathode side of the Swagelok cell, which permited O_2 to flow in and participated into the reaction of cathode. Moreover, the Li-O_2 batteries with LRu@NC and NC cathodes were assembled under the same condition. Tests were carried out in a glove box filled with pure oxygen. LAND cycler (Wuhan Land Electronic Co. Ltd.) was used for electrochemical investigation.

3 Results and discussion

3.1 Characterization of LRu@HDCo-NC

Figure 1(a) gives the schematic diagram for preparing the Ru coating Co-based material. As shown in Fig. 1(a), Co and Zn-based nitrates were firstly mixed together in the methanol and then reacted with dimethyl imidazole (MeIm) by the seed-mediated growth method to synthesize Co/Zn-ZIFs. Subsequently, the $Ru(acac)_3$ organic molecules were absorbed into the ordered mesopores of Co/Zn-ZIFs. It should be noted that these mesoporous channels can effectively confine Ru-based sites to inhibit their aggregation over the pyrolysis process. The as-prepared $Ru(acac)_3$@Co/Zn-ZIFs were treated at 900 °C for 3 h under the N_2 atmosphere. During the carbonization process, Zn metal volatilized at the high temperature to produce the plentiful pores and optimized the N-based phases on the surface. At the same time, some Co/Zn centers were easily replaced by the Ru ions, which could be linked with N-based ligands and then reduced to Ru-based nanoparticles. Finally, the highly dispersed Co-based nanoparticles encapsulated into porous N-doping carbon polyhedron with LRu@NC were obtained after cooling (named as LRu@HDCo-NC). The morphology and structure of the obtained LRu@HDCo-NC, LRu@NC, NC, and their precursors were firstly characterized by scanning electron

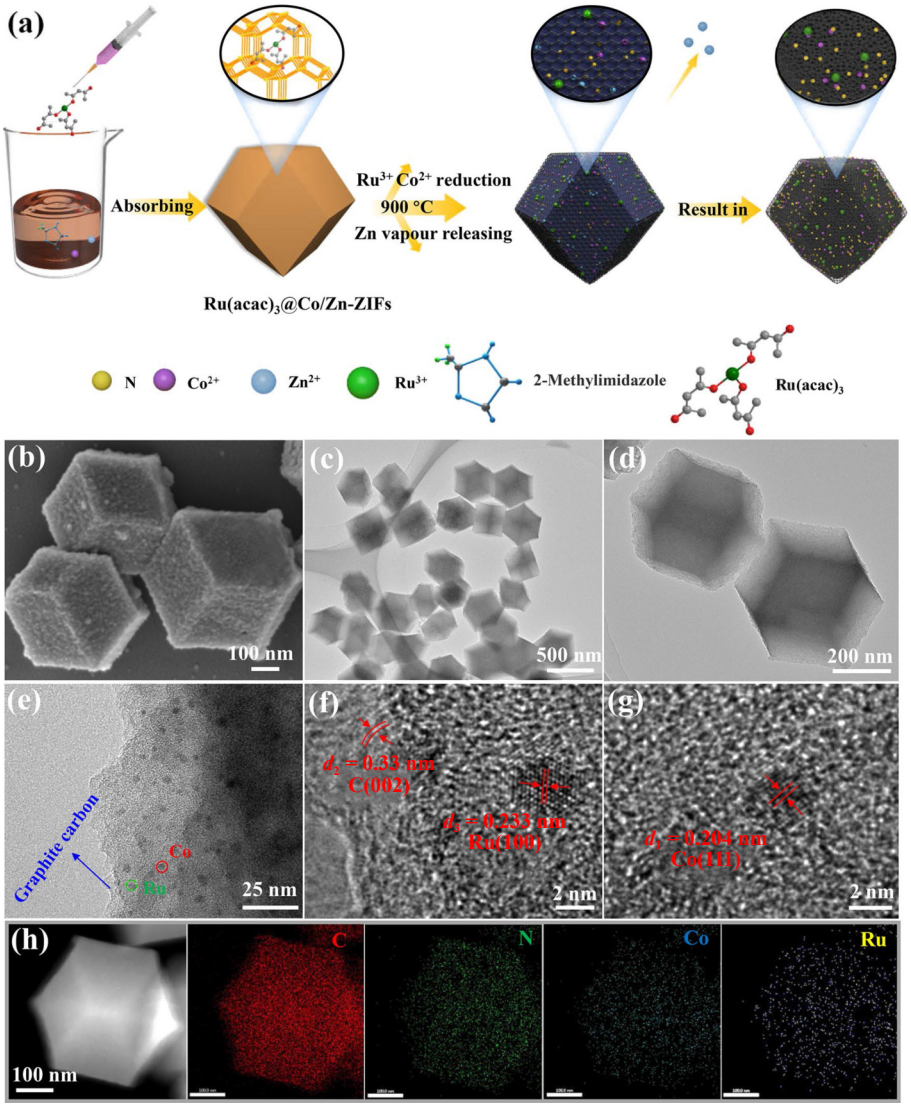

Figure 1 (a) Schematic illustration of the preparation steps for LRu@HDCo-NC. (b) SEM and ((c) and (d)) TEM images of LRu@HDCo-NC with different magnifications. (e)–(g) HR-TEM image of LRu@HDCo-NC. (h) TEM image of LRu@HDCo-NC and the corresponding EDX mapping images of C, N, Co, and Ru elements, respectively.

microscope (SEM) and transmission electron microscopy (TEM). This phenomenon suggests that the high-temperature carbonization does not destroy the basic structure of ZIFs framework. Although LRu@HDCo-NC exhibits the relatively rough surface, there is rarely any agglomeration of metal-based active sites on the surface (Fig. 1(b)).

The TEM images of LRu@HDCo-NC shown in Figs. 1(c) and 1(d) indicate that they have the well-maintained dodecahedral texture and there are almost no large particles in their framework as well as in LRu@NC and NC (Fig. S3 in the ESM). In the high-resolution (HR) TEM image (Fig. 1(e)), the distribution of metal-based nanoparticles in the LRu@HDCo-NC is ultra-small and very uniform. Figures 1(f) and 1(g) further present that the diameter of the nanoparticles in the LRu@HDCo-NC dodecahedrons is almost all 2 nm and these ultra-small particles show clear lattice fringes with spacing of 0.204, 0.330, and 0.233 nm, which correspond to (111) plane of Co, (002) plane of graphitic carbon, and (100) plane of metallic Ru, respectively. These results reveal the successful introduction of the small-size and uniformly dispersed Ru and Co species in LRu@HDCo-NC. The energy-dispersive X-ray (EDX) mapping technology was also applied to detect the elemental distribution of LRu@HDCo-NC. It can be obversed from Fig. 1(h) that Ru, Co, N, and C elements are uniformly distributed in LRu@HDCo-NC. Moreover, the inductively coupled plasma-optical emission spectroscopy (ICP-OES) analysis confirms that the overall Ru percentage is 1.8 wt.% in LRu@HDCo-NC (Table S1 in the ESM), which is lower than many recently reported nobal-based catalysts (Table S2 in the ESM).

The crystal structure and phase composition of LRu@HDCo-NC, LRu@NC, NC, and their precursors were confirmed by X-ray diffraction (XRD) technology. All the diffraction peaks of $Ru(acac)_3$@Co/Zn-ZIFs, $Ru(acac)_3$@Zn-ZIFs and Zn-ZIFs are well matched with ZIF-8 (Fig. S4 in the ESM), suggesting the successful synthesis of these ZIF precursors. The LRu@HDCo-NC, LRu@NC, and NC derivatives all exhibit the peaks at 25° and 44° (Fig. 2(a)), which are attributed to the planes (002) and (101) of graphite carbon. However, there are no Ru or Co-related peaks in the XRD patterns of LRu@HDCo-NC and LRu@NC, suggesting that the Co and Ru phases in these derivatives are less-cystral. The Raman spectra shown in Fig. S5 in the ESM suggest the co-existence of Ru- and Co-based sites in LRu@HDCo-NC effectively enhances the amounts of defective carbons which are beneficial to the catalytic performance. To further analyze the surface elemental composition and chemical state of these catalysts, the X-ray photoelectron spectroscopy (XPS) measurement was also conducted. Compared with LRu@NC and NC, apart from the co-existence of C, N, O, and Ru species, there are also Co species in

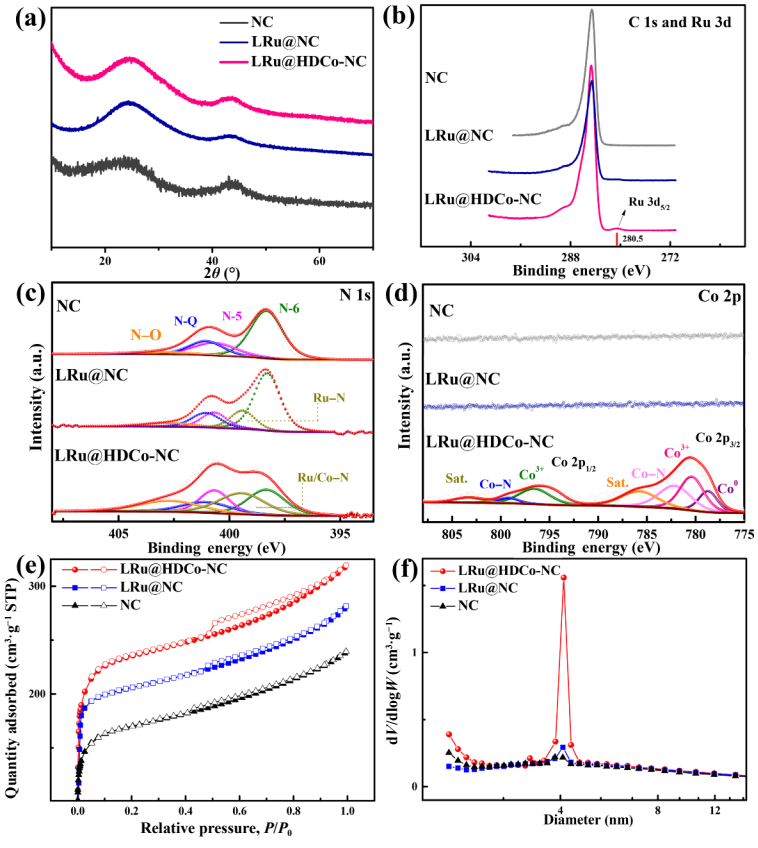

Figure 2 (a) XRD patterns of LRu@HDCo-NC, LRu@NC, and NC. (b) The comparisons of the high-resolution XPS spectra of (b) C 1s, (c) N 1s and (d) Co 2p for three NC-based derivatives. (e) N_2 adsorption and desorption isotherms and (f) pore-size distributions of LRu@HDCo-NC, LRu@NC, and NC.

the full XPS spectra of LRu@HDCo-NC (Fig. S6 in the ESM). It can be found from Fig. 2(b) and Fig. S7 in the ESM that the Ru species have been successfully introduced into the LRu@NC and LRu@HDCo-NC. Additionally, it is worth noting that the high-resolution N 1s XPS spectra of LRu@NC and LRu@HDCo-NC both have five types of N sub-peaks: pyridinic N (N-6) at 398.4 eV, metal–N (M–N) at 399.4 eV, pyrrolic N (N-5) at 400.7 eV, graphitic N (N-Q) at 401.1 eV, and oxidized-N (N–O) at 402.8 eV, while the high-resolution N 1s XPS spectra of NC can only be deconvoluted into four sub-peaks (including N-6, N-5, N-Q, and N-O) (Fig. 2(c)), which further suggests the existence of the N-coordinated Co or Ru sites in LRu@NC and LRu@HDCo-NC [38–40]. Compared with LRu@NC, LRu@HDCo-NC shows the higher content percentage of M–N (24.59%) on the surface (Table S3 in the ESM), indirectly indicating that both Ru and Co species can bond with N in LRu@HDCo-NC which have been confirmed to greatly enhance catalytic performance [41, 42]. It can be further observed from Fig. 2(d) that only LRu@HDCo-NC has the co-existence of metallic Co (778.7 eV), Co-N (782.2 and 799.2 eV), and Co^{3+} (780.5 and 796.60 eV) species. The N_2 adsorption–desorption tests have also been implemented to explore the surface properties and pore texture of three NC-based particles. All the N_2 adsorption–desorption curves of LRu@HDCo-NC, LRu@NC, and NC samples show the typical IV isotherms: the distinct increasing N_2 adsorption–desorption curves at the low relative pressure (P/P_0 < 0.05) which are corresponding to micropores and the typical hysteresis loops under the higher relative pressure range (P/P_0: 0.4–1.0) which reflect the existence of mesopores (Fig. 2(e)). The pore-size distribution shown in Fig. 2(f) further confirms the hierarchical pores in the three derivative catalysts. Furthermore, among three NC-based derivatives, LRu@HDCo-NC exhibits the highest Brunauer–Emmett–Teller (BET) surface area (S_{BET}) of 735.09 $m^2 \cdot g^{-1}$ and the largest pore volume of 0.4964 $cm^3 \cdot g^{-1}$ (Table S4 in the ESM), suggesting that the synergy between Zn vapour releasing and Ru introduction ensure the formation of plentiful pores during pyrolysis. The large surface area and highly porous structure of LRu@HDCo-NC are good for the Li-O_2 batteries since the recent reports have demonstrated that the optimized pores in catalyst can not only facilitate O_2 infusion and electrolyte infiltration in Li-O_2 batteries performance, but also provide adequate space to induce reversible formation/decomposition of discharge products Li_2O_2 in Li-O_2 batteries [43–47].

3.2 Electrochemical performance of Li-O_2 battery with LRu@HDCo-NC cathode

To elucidate the catalytic activity of the LRu@HDCo-NC cathode, the cyclic voltammetry (CV) and galvanostatic discharge/charge tests were carried out. For comparison, the LRu@NC and NC catalysts were also tested under the same conditions. Figure 3(a) gives the CV profiles of the Li-O_2 batteries with LRu@HDCo-NC, LRu@NC, and NC cathode between 2.0 and 4.5 V at a scan rate of 0.1 $mV \cdot s^{-1}$. As shown in Fig. 3(a), the oxygen reduction onset potential of the LRu@NC cathode (~ 2.84 V) is slightly higher compared with that of the NC electrode (~ 2.81 V), indicating that Ru-N species accelerate the ORR kinetics. It should be noted that the O_2 reduction onset potential of the LRu@HDCo-NC cathode is as high as 2.91 V which is close to the theoretical value of Li_2O_2 formation (2.96 V). This phenomenon confirms that the co-existence of Co and Ru species greatly increases the catalytic performance of LRu@HDCo-NC [48]. On the other hand, the LRu@HDCo-NC cathode further shows two anodic peaks at around 3.26 and 4.2 V, respectively, which can be attributed to the delithiation and the oxidation reaction [49–51]. On the contrast, the oxidation peaks in the CV profiles of the LRu@NC and NC cathodes are relatively low. These results indicate that the LRu@HDCo-NC electrode shows the enhanced OER

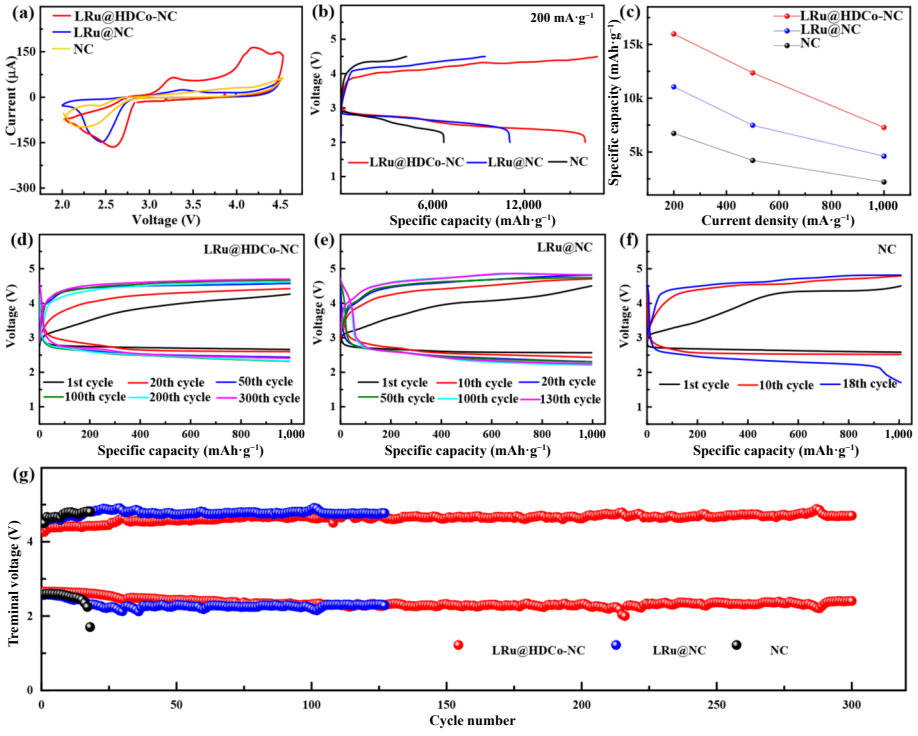

Figure 3 (a) CV curves at a scan rate of 0.1 mV·s^{-1}, (b) full discharge/charge curves in a range of 2–4.5 V at 200 mA·g^{-1} and (c) discharge capacities comparison at the different densities of Li-O_2 batteries based on of LRu@HDCo-NC, LRu@NC, and NC cathodes. Cycling performance of (d) LRu@HDCo-NC, (e) LRu@NC, and (f) NC cathodes with a fixed capacity of 1, 000 mAh·g^{-1} at 500 mA·g^{-1}, and (g) their corresponding terminal voltages vs. the cycle number.

performance and thus promotes the decomposition of discharge products at low charge potential. Figure 3(b) presents the full discharge/charge curves of the Li-O_2 batteries using LRu@HDCo-NC, LRu@NC, and NC electrodes at 200 mA·g^{-1} with the voltage window of 2.0–4.5 V, respectively. It can be found from Fig. 3(b) that the discharge capacity of the LRu@HDCo-NC cathode is 15,973 mAh·g^{-1} at 200 mA·g^{-1}, which is higher than the LRu@NC electrode (11,058 mAh·g^{-1}) and the NC electrode (6,733 mAh·g^{-1}). During the charging process, a reversible recharge capacity (16,766 mAh·g^{-1}) is achieved for the LRu@HDCo-NC cathode, while the LRu@NC and NC cathodes only deliver the limited recharge capacities of 9,427 and 4,284 mAh·g^{-1}, respectively. Even at 500 mA·g^{-1}, the Li-O_2 batteries with LRu@HDCo-NC cathode also show outstanding capacity retention (Fig. S8 in the ESM). In addition, the specific capacities of the LRu@HDCo-NC, LRu@NC, and NC based Li-O_2 batteries at different applied current densities were also investigated (Fig. 3(c)). It can be observed from Fig. 3(c) and Fig. S8 in the ESM that the discharge capacity of the LRu@HDCo-NC cathode can reach 12,362 mAh·g^{-1} at 500 mA·g^{-1}, which is larger than these of the batteries with LRu@NC (7,483 mAh·g^{-1}) and NC (4,215 mAh·g^{-1}) cathodes, respectively. Even at the higher current of 1,000 mA·g^{-1}, the LRu@HDCo-NC cathode still maintians a discharge capacity of 7,281 mAh·g^{-1}, while the capacities of the LRu@NC and NC cathodes sharply drop down to 4,608 and 2,208 mAh·g^{-1} (Fig. 3(c) and Fig. S9(a) in the ESM), respectively. These results confirm the outstanding rate performance of the LRu@HDCo-NC-based Li-O_2 battery. To further confirm the cycling stability of the three NC-based catalysts, the continuous discharge–charge profiles of the Li-O_2 batteries with the LRu@HDCo-NC, LRu@NC, or NC electrodes have also been studied at 500 mA·g^{-1} with a fixed capacity of 1,000 mAh·g^{-1} since the fixed specific capacity strategy can suppress overgrowth of products on the cathode [52]. As shown in Fig. 3(d), the Li-O_2 battery using the LRu@HDCo-NC cathode can be stably operated over 300 cycles, which is much better than most of the recently reported Li-O_2 batteries (Table S5 in the ESM). However, the LRu@NC and NC cathodes show the apparent decay after 130 and 18 cycles, respectively (Figs. 3(e) and 3(f)). It can be seen from Fig. 3(g) and Fig. S9(b) in the ESM that the voltage gap between discharge and charge terminal potential of the LRu@HDCo-NC cathode at the first cycle (only 1.58 V) is much lower compared with the LRu@NC and NC cathode and even could maintain below 2.3 V at the 300th cycle. On the contrast, the average overpotentials obtained at the end of the discharge and charge curves of the LRu@NC cathode can reach ~ 2.42 V during the whole cycling. For the NC eletrode, the terminal discharge voltage shows obviously drop after only 18 continuous cycles. Moreover, the corresponding potential gaps between discharge terminal and charge terminal are as high as 3.1 V at the 18th cycle for the NC-based Li-O_2 cell (Fig. 3(g)). These above results further demonstrate that the synergy of the highly dispered Ru and Co nanoparticles with low content in LRu@HDCo-NC effectively improves the revesible formation/decomposition of Li_2O_2 in Li-O_2 batteries. However, it should be noted that there are the fluctuations of the discharge/charge terminal voltage during cycling for three NC-based cathodes (Figs. 3(d)–3(g)), which may be attributed to the ambient temperature/O_2 changes and so on. Interestingly, the highly dispersed Co-based nanoparticles encapsulated into porous N-doping carbon polyhedral with the low content of Pt modification (LPt@HDCo-NC) have been also prepared for comparison and the obtained LPt@HDCo-NC cathode shows the inferior cycling performance compared with the LRu@HDCo-NC cathode (Fig. S10 in the ESM), which further indicates the superiority of Ru species in Li-O_2 batteries.

3.3 Products analysis of Li-O_2 battery using LRu@HDCo-NC cathode

To clarify the reasons for the excellent performance of Li-O_2 battery with LRu@HDCo-NC cathode, a series of characterizations, including *ex situ* SEM, XRD, Fourier transform-infrared spectroscopy (FTIR), electrochemical impedance

spectroscopy (EIS), and *in situ* differential electrochemical mass spectrometry (DEMS) were conducted. Figures 4(a)–4(f) show the morphology evolution of the LRu@HDCo-NC cathodes under different discharge/charge states. Compared with the pristine LRu@HDCo-NC electrode (Figs. 4(a) and 4(d)), the discharged LRu@HDCo-NC cathode is covered with many nanosheet-like discharge products on the surface (Figs. 4(b) and 4(e)), which are consistent with the recent reports [53, 54]. Moreover, recent work also has confirmed that the nanosheet-like products should be easily decomposed, which are beneficial to battery performance [55]. After fully recharged, these nanosheets completely vanish and the original dodecahedrons can be identified clearly (Figs. 4(c) and 4(f)) on the cathode, indicating the good stability of LRu@HDCo-NC. EIS data shown in Fig. S11 in the ESM also confirm the remarkable electrochemical properties of LRu@HDCo-NC. Figure 5(a) gives the XRD patterns of the LRu@HDCo-NC cathodes at the pristine, discharged, and charged stages, respectively. As shown in Fig. 5(a), the characteristic peaks related to Li_2O_2 emerge at the end of discharge and subsequently disappear after recharge on the LRu@HDCo-NC electrodes. Moreover, *ex situ* FTIR also confirms the formation of Li_2O_2 during discharging process and its subsequent decomposition over following recharging process on the LRu@HDCo-NC cathode (Fig. 5(b)). To further study the reversibility of Li-O_2 cell with LRu@HDCo-NC cathode, *in situ* DEMS measurement was also employed to monitor the gas evolution during cycling. Customized Swagelok cell was connected to a commercial quadrupole mass spectrometer (Fig. S12 in the ESM). In this experiment, each sealed cell with LRu@HDCo-NC cathode was firstly purged with the mixed gas of O_2/Ar (the volume ratio of O_2/Ar was 0.25) for 8 h until the flow steady. Afterwards, the above cell was discharged at a current of 300 μA for 2 h. After discharge, the cell was kept under a purge Ar stream for 7 h to remove residual O_2. Then, the system was recharged at a current of 300 μA for 2 h in the purge Ar stream. The online gas analysis was also carried out throughout the whole testing process. For comparison, LRu@NC and NC cathodes were also examined by *in situ* DEMS test under the same condition. Figures 5(c) and 5(d) and Fig. S13 in the ESM deliver the typical galvanostatic discharge/charge profiles of Li-O_2 cells with LRu@HDCo-NC or LRu@NC cathodes and the corresponding gas evolution during cycling. Over discharging, LRu@NC cathode shows the lower voltage platforms compared with LRu@HDCo-NC cathode and the corresponding DEMS data also explicitly indicate that O_2 is steadily consumed for both electrodes (Fig. 5(c) and Fig. S13(a) in the ESM). During charging, the overpotential of the LRu@NC cathode is higher than that of the LRu@HDCo-NC cathode, demonstrating that the additional introduction of the highly dispersed Co nanoparticles is beneficial to improving OER in Li-O_2 cells. Although the generated O_2 and CO_2 gases can be detected for both Ru based-cathodes, the amount of the evolved CO_2 at the LRu@NC cathode is more obvious than that at the LRu@HDCo-

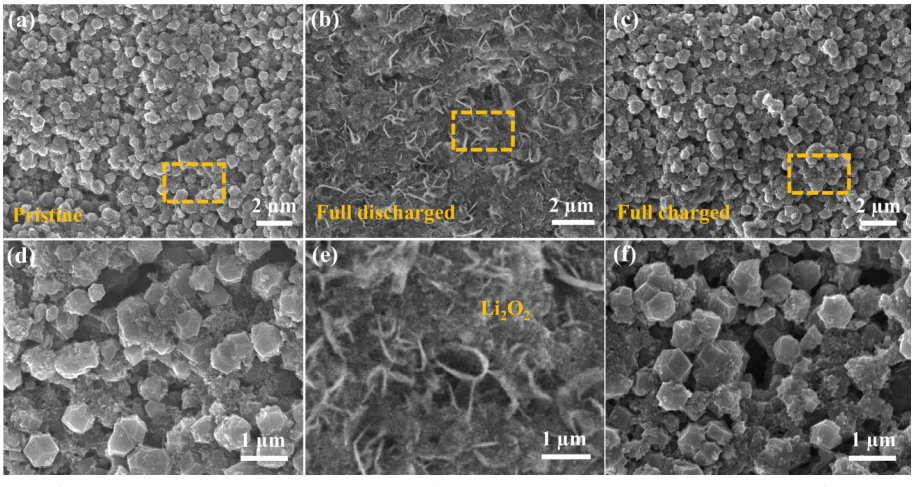

Figure 4 *Ex-situ* SEM images of the LRu@HDCo-NC cathodes at the ((a) and (d)) pristine, ((b) and (e)) discharged, and ((c) and (f)) charged stages.

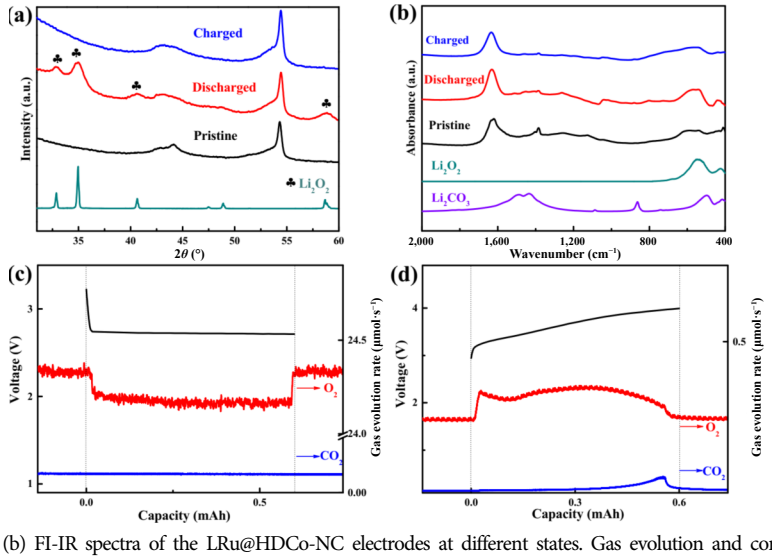

Figure 5 (a) XRD patterns and (b) FI-IR spectra of the LRu@HDCo-NC electrodes at different states. Gas evolution and corresponding voltage curves of the LRu@HDCo-NC based Li-O_2 battery at 0.3 mA with limited capacity of 0.6 mAh over the (c) discharging and (d) charging processes.

NC cathode (Fig. 5(d) and Fig. S13(b) in the ESM)). Additionally, the *in-situ* DEMS data of the NC cathode shown in Fig. S14 in the ESM indicate that the Ru introduction can efficiently suppress side reactions in Li-O_2 batteries. Moreover, the electrons (e^-) per oxygen molecule (O_2) consumption of the LRu@HDCo-NC based Li-O_2 cell over discharge can reach 2.04, while the corresponding e^-/O_2 over recharge at the LRu@HDCo-NC cathode is 2.23, which suggests the Li_2O_2/O_2 conversion dominates the discharge/charge progress in Li-O_2 batteries using LRu@HDCo-NC cathode. However, it should be noted that the ratio of e^-/O_2 during discharge for the LRu@NC and NC cathodes is 2.15 and 2.18, while the e^-/O_2 ratio for the LRu@NC and NC electrodes over recharge is 2.9 and 5.4, respectively (Figs. S13 and S14 in the ESM). The above results further demonstrate that the synergy of Co and Ru nanoparticles effectively enhances the reversibility of Li-O_2 batteries.

4 Conclusions

In summary, we synthesized the Co/Zn-ZIFs by seed-mediated method and further applied its ordered mesoporous channels to absorb Ru-containing ligands to obtain Ru(acac)$_3$@Co/Zn-ZIFs. Through the high temperature pyrolysis, the highly dispersed Co-based nanoparticles encapsulated into porous N-doping carbon polyhedral with the low content of Ru modification (LRu@HDCo/NC) were prepared and further used in Li-O_2 battery. The LRu@HDCo-NC based Li-O_2 battery exhibits a super-high discharged capacity (15,973 mAh·g^{-1}) at 200 mA·g^{-1} with the high coulombic efficiency and the perfect rate performance (12,362 mAh·g^{-1} at the current density of 500 mA·g^{-1} and 7,281 mAh g^{-1} at 1,000 mA·g^{-1}) under the full discharge/charge test. Even operating at the fixed capacity of 1,000 mAh·g^{-1}, the Li-O_2 battery with the LRu@HDCo-NC cathode shows the long cycling life (300 cycles) with the stable overpotential of below 2.3 V. *Ex-situ* SEM, FTIR, XRD, and *in-situ* DEMS technologies have also been applied and strongly confirm that LRu@HDCo-NC cathode can effectively promote the reversible formation/decomposition of Li_2O_2 during the discharge–charge process. The excellent electrochemical performances of the LRu@HDCo-NC catalyst in Li-O_2 batteries can be attributed to its unique structure and composite. Due to the Zn species adjustment, the LRu@HDCo-NC possesses the plentiful porous channels, enhanced surface N content, and the highly distributed active sites. In addition, the stable and porous carbon framework not only improves the conductivity and catalytic performance towards ORR of the LRu@HDCo-NC catalyst, but also provides the high-efficient O_2/ions transfer channels and buffer spaces to optimize the formation of Li_2O_2 particles. Moreover, even with the very low content of Ru, the synergy between the highly dispersed Co and Ru-based particles greatly enhances the OER property of LRu@HDCo-NC to reduce the overpotential and further alleviate the electrolyte/electrode decomposition in Li-O_2 batteries over cycles. Our work presented here paves an effective and simple way to construct the high-efficient catalysts not only for the Li-O_2 batteries, but also for other metal-air cells (such as Na-air or Zn-air systems).

Acknowledgements

The authors acknowledge funding support from the National Natural Science Foundation of China (Nos. 21905151 and 51772162), Youth Innovation and Technology Foundation of Shandong Higher Education Institutions, China (No. 2019KJC004), Outstanding Youth Foundation of Shandong Province, China (No. ZR2019JQ14), Taishan Scholar Young Talent Program, Major Scientific and Technological Innovation Project (No. 2019JZZY020405), and the Postdoctoral Science Foundation of China (No. 2019M652499).

Electronic Supplementary Material: Supplementary material (materials, the preparation of contrast samples, characterization instrumentation, TEM images, SEM images, XRD pattern, EIS spectra of samples, Raman spectroscopy, XPS spectra, discharge/charge curves, ICP-OES, DEMS, and cycling performance) is available in the online version of this article at https://doi.org/10.1007/s12274-021-3938-2.

References

[1] Kong, L. J.; Zhong, M.; Shuang, W.; Xu, Y. H.; Bu, X. H. Electrochemically active sites inside crystalline porous materials for energy storage and conversion. *Chem. Soc. Rev.* **2020**, *49*, 2378–2407.

[2] Kwak, W. J.; Rosy; Sharon, D.; Xia, C.; Kim, H.; Johnson, L. R.; Bruce, P. G.; Nazar, L. F.; Sun, Y. K.; Frimer, A. A. et al. Lithium-oxygen batteries and related systems: Potential, status, and future. *Chem. Rev.* **2020**, *120*, 6626–6683.

[3] Harper, G.; Sommerville, R.; Kendrick, E.; Driscoll, L.; Slater, P.; Stolkin, R.; Walton, A.; Christensen, P.; Heidrich, O.; Lambert, S. et al. Recycling lithium-ion batteries from electric vehicles. *Nature* **2019**, *575*, 75–86.

[4] Gao, H. N.; Gallant, B. M. Advances in the chemistry and applications of alkali-metal-gas batteries. *Nat. Rev. Chem.* **2020**, *4*, 566–583.

[5] Luo, Z. K.; Liang, C. S.; Wang, F.; Xu, Y. H.; Chen, J.; Liu, D.; Sun, H. Y.; Yang, H.; Fan, X. P. Optimizing main materials for a lithium-air battery of high cycle life. *Adv. Funct. Mater.* **2014**, *24*, 2101–2105.

[6] Chi, X. W.; Li, M. L.; Di, J. C.; Bai, P.; Song, L. N.; Wang, X. X.; Li, F.; Liang, S.; Xu, J. J.; Yu, J. H. A highly stable and flexible zeolite electrolyte solid-state Li-air battery. *Nature* **2021**, *592*, 551–557.

[7] Chen, L.; Chen, Z.; Liu, X. D.; Wang, X. L. Bimetallic metal-organic framework derived doped carbon nanostructures as high-performance electrocatalyst towards oxygen reactions. *Nano Res.* **2021**, *14*, 1533–1540.

[8] Wang, C. Y.; Zhang, Z. H.; Liu, W. W.; Zhang, Q. M.; Wang, X. G.; Xie, Z. J.; Zhou, Z. Enzyme-inspired room-temperature lithium-oxygen chemistry via reversible cleavage and formation of dioxygen bonds. *Angew. Chem., Int. Ed.* **2020**, *59*, 17856–17863.

[9] Nai, J. W.; Zhao, X. Y.; Yuan, H. D.; Tao, X. Y.; Guo, L. Amorphous carbon-based materials as platform for advanced high-performance anodes in lithium secondary batteries. *Nano Res.* **2021**, *14*, 2053–2066.

[10] Lee, J. S.; Kim, S. T.; Cao, R. G.; Choi, N. S.; Liu, M. L.; Lee, K. T.; Cho, J. Metal-air batteries with high energy density: Li-air versus Zn-air. *Adv. Energy Mater.* **2011**, *1*, 34–50.

[11] Gao, X. W.; Chen, Y. H.; Johnson, L. R.; Jovanov, Z. P.; Bruce, P. G. A rechargeable lithium-oxygen battery with dual mediators stabilizing the carbon cathode. *Nat. Energy* **2017**, *2*, 17118.

[12] Zhou, B.; Guo, L. M.; Zhang, Y. T.; Wang, J. W.; Ma, L. P.; Zhang, W. H.; Fu, Z. W.; Peng, Z. Q. A high-performance Li-O_2 battery with a strongly solvating hexamethylphosphoramide electrolyte and a LiPON-protected lithium anode. *Adv. Mater.* **2017**, *29*, 1701568.

[13] Bi, X. X.; Li, M.; Liu, C.; Yuan, Y. F.; Wang, H.; Key, B.; Wang, R. Y.; Shahbazian-Yassar, R.; Curtiss, L. A.; Lu, J. et al. Cation additive enabled rechargeable LiOH-based lithium-oxygen batteries. *Angew. Chem., Int. Ed.* **2020**, *59*, 22978–22982.

[14] Qiao, Y.; Wang, Q. F.; Mu, X. W.; Deng, H.; He, P.; Yu, J. H.; Zhou, H. S. Advanced hybrid electrolyte Li-O_2 battery realized by dual superlyophobic membrane. *Joule* **2019**, *3*, 2986–3001.

[15] Lim, H. D.; Lee, B.; Bae, Y.; Park, H.; Ko, Y.; Kim, H.; Kim, J.; Kang, K. Reaction chemistry in rechargeable Li-O_2 batteries. *Chem. Soc. Rev.* **2017**, *46*, 2873–2888.

[16] Qiao, Y.; Yi, J.; Guo, S. H.; Sun, Y.; Wu, S. C.; Liu, X. Z.; Yang, S.

X.; He, P.; Zhou, H. S. Li_2CO_3-free Li-O_2/CO_2 battery with peroxide discharge product. *Energy Environ. Sci.* **2018**, *11*, 1211–1217.

[17] Dai, L. N.; Sun, Q.; Chen, L. N.; Guo, H. H.; Nie, X. K.; Cheng, J.; Guo, J. G.; Li, J. W.; Lou, J.; Ci, L. J. Ag doped urchin-like α-MnO_2 toward efficient and bifunctional electrocatalysts for Li-O_2 batteries. *Nano Res.* **2020**, *13*, 2356–2364.

[18] Peng, Z. Q.; Freunberger, S. A.; Hardwick, L. J.; Chen, Y. H.; Giordani, V.; Bardé, F.; Novák, P.; Graham, D.; Tarascon, J. M.; Bruce, P. G. Oxygen reactions in a non-aqueous Li^+ electrolyte. *Angew. Chem., Int. Ed.* **2011**, *50*, 6351–6355.

[19] Xu, S. M.; Liang, X.; Wu, X. Y.; Zhao, S. L.; Chen, J.; Wang, K. X.; Chen, J. S. Multistaged discharge constructing heterostructure with enhanced solid-solution behavior for long-life lithium-oxygen batteries. *Nat. Commun.* **2019**, *10*, 5810.

[20] Gong, H.; Wang, T.; Xue, H. R.; Lu, X. Y.; Xia, W.; Song, L.; Zhang, S. T.; He, J. P.; Ma, R. Z. Spatially-controlled porous nanoflake arrays derived from MOFs: An efficiently long-life oxygen electrode. *Nano Res.* **2019**, *12*, 2528–2534.

[21] Liu, T.; Vivek, J. P.; Zhao, E. W.; Lei, J.; Garcia-Araez, N.; Grey, C. P. Current challenges and routes forward for nonaqueous lithium-air batteries. *Chem. Rev.* **2020**, *120*, 6558–6625.

[22] Lai, J. N.; Xing, Y.; Chen, N.; Li, L.; Wu, F.; Chen, R. J. Electrolytes for rechargeable lithium-air batteries. *Angew. Chem., Int. Ed.* **2020**, *59*, 2974–2997.

[23] Zhang, P.; Ding, M. J.; Li, X. X.; Li, C. X.; Li, Z. Q.; Yin, L. W. Challenges and strategy on parasitic reaction for high-performance nonaqueous lithium-oxygen batteries. *Adv. Energy Mater.* **2020**, *10*, 2001789.

[24] Luo, J. R.; Yao, X. H.; Yang, L., Han, Y.; Chen, L.; Geng, X. M.; Vattipalli, V.; Dong, Q.; Fan, W.; Wang, D. W.; Zhu, H. L. Free-standing porous carbon electrodes derived from wood for high-performance Li-O_2 battery applications. *Nano Res.* **2017**, *10*, 4318–4326.

[25] Shu, C. Z.; Wang, J. Z.; Long, J. P.; Liu, H. K.; Dou, S. X. Understanding the reaction chemistry during charging in aprotic lithium-oxygen batteries: Existing problems and solutions. *Adv. Mater.* **2019**, *31*, 1804587.

[26] Liu, T.; Wang, L. D. Y.; Huang, T.; Yu, A. S. Well-defined carbon nanoframes containing bimetal-N-C active sites as efficient bi-functional electrocatalysts for Li-O_2 batteries. *Nano Res.* **2019**, *12*, 517–523.

[27] Li, M.; Bi, X. X.; Wang, R. Y.; Li, Y. B.; Jiang, G. P.; Li, L.; Zhong, C.; Chen, Z. W.; Lu, J. Relating catalysis between fuel cell and metal-air batteries. *Matter* **2020**, *2*, 32–49.

[28] Zhang, Y. Q.; Tao, L.; Xie, C.; Wang, D. D.; Zou, Y. Q.; Chen, R.; Wang, Y. Y.; Jia, C. K.; Wang, S. Y. Defect engineering on electrode materials for rechargeable batteries. *Adv. Mater.* **2020**, *32*, 1905923.

[29] Mu, X. W.; Wen, Q. H.; Ou, G.; Du, Y. M.; He, P.; Zhong, M. L.; Zhu, H.; Wu, H.; Yang, S. X.; Liu, Y. J. et al. A current collector covering nanostructured villous oxygen-deficient NiO fabricated by rapid laser-scan for Li-O_2 batteries. *Nano Energy* **2018**, *51*, 83–90.

[30] Mu, X. W.; Jiang, J.; Deng, H.; Qiao, Y.; Zheng, M. B.; Zhang, X. P.; He, P.; Zhou, H. S. H_2O self-trapping air cathode of Li-O_2 battery enabling low charge potential operating in dry system. *Nano Energy* **2019**, *64*, 103945.

[31] Liu, T.; Huang, T.; Yu, A. S. Rational design of a hierarchical N-doped graphene-supported catalyst for highly energy-efficient lithium-oxygen batteries. *J. Mater. Chem. A* **2019**, *7*, 19745–19752.

[32] Zhao, R.; Liang, Z. B.; Zou, R. Q.; Xu, Q. Metal-organic frameworks for batteries. *Joule* **2018**, *2*, 2235–2259.

[33] Jiang, Z. L.; Sun, H.; Shi, W. K.; Zhou, T. H.; Hu, J. Y.; Cheng, J. Y.; Hu, P. F.; Sun, S. G. Co_3O_4 nanocage derived from metal-organic frameworks: An excellent cathode catalyst for rechargeable Li-O_2 battery. *Nano Res.* **2019**, *12*, 1555–1562.

[34] Lyu, Z. Y.; Lim, G. J. H.; Guo, R.; Kou, Z. K.; Wang, T. T.; Guan, C.; Ding, J.; Chen, W.; Wang, J. 3D-Printed MOF-derived hierarchically porous frameworks for practical high-energy density Li-O_2 Batteries. *Adv. Funct. Mater.* **2019**, *29*, 1806658.

[35] Chao, F. F.; Wang, B. X.; Ren, J. J.; Lu, Y. W.; Zhang, W. R.; Wang, X. Z.; Cheng, L.; Lou, Y. B.; Chen, J. X. Micro-meso-macroporous FeCo-N-C derived from hierarchical bimetallic FeCo-ZIFs as cathode catalysts for enhanced Li-O_2 batteries performance. *J. Energy Chem.* **2019**, *35*, 212–219.

[36] Jian, Z. L.; Liu, P.; Li, F. J.; He, P.; Guo, X. W.; Chen, M. W.; Zhou, H. S. Core-shell-structured CNT@RuO_2 composite as a high-performance cathode catalyst for rechargeable Li-O_2 batteries. *Angew. Chem., Int. Ed.* **2014**, *53*, 442–446.

[37] Hu, X. L.; Luo, G.; Zhao, Q. N.; Wu, D.; Yang, T. X.; Wen, J.; Wang, R. H.; Xu, C. H.; Hu, N. Ru single atoms on N-doped carbon by spatial confinement and ionic substitution strategies for high-performance Li-O_2 batteries. *J. Am. Chem. Soc.* **2020**, *142*, 16776–16786.

[38] Huang, K. X.; Zhang, W. Q.; Li, J.; Fan, Y. J.; Yang, B.; Rong, C. Y.; Qi, J. H.; Chen, W.; Yang, J. *In situ* anchoring of zeolite imidazole framework-derived Co, N-doped porous carbon on multiwalled carbon nanotubes toward efficient electrocatalytic oxygen reduction. *ACS Sustainable Chem. Eng.* **2019**, *8*, 478–485.

[39] Ren, W. H.; Tan, X.; Yang, W. F.; Jia, C.; Xu, S. M.; Wang, K. X.; Smith, S. C.; Zhao, C. Isolated diatomic Ni-Fe metal-nitrogen sites for synergistic electroreduction of CO_2. *Angew. Chem., Int. Ed.* **2019**, *58*, 6972–6976.

[40] Wang, J.; Yin, Y. B.; Liu, T.; Yang, X. Y.; Chang, Z. W.; Zhang, X. B. Hybrid electrolyte with robust garnet-ceramic electrolyte for lithium anode protection in lithium-oxygen batteries. *Nano Res.* **2018**, *11*, 3434–3441.

[41] Liang, Z. Z.; Kong, N. N.; Yang, C. X.; Zhang, W.; Zheng, H. Q.; Lin, H. P.; Cao, R. Highly curved nanostructure-coated Co, N-doped carbon materials for oxygen electrocatalysis. *Angew. Chem., Int. Ed.* **2021**, *60*, 12759–12764.

[42] Wang, P.; Ren, Y. Y.; Wang, R. T.; Zhang, P.; Ding, M. J.; Li, C. X.; Zhao, D. Y.; Qian, Z.; Zhang, Z. W.; Zhang, L. Y. et al. Atomically dispersed cobalt catalyst anchored on nitrogen-doped carbon nanosheets for lithium-oxygen batteries. *Nat. Commun.* **2020**, *11*, 1576.

[43] Luo, N.; Ji, G. J.; Wang, H. F.; Li, F.; Liu, Q. C.; Xu, J. J. Process for a free-standing and stable all-metal structure for symmetrical lithium-oxygen batteries. *ACS Nano* **2020**, *14*, 3281–3289.

[44] Guan, D. H.; Wang, X. X.; Li, M. L.; Li, F.; Zheng, L. J.; Huang, X. L.; Xu, J. J. Light/electricity energy conversion and storage for a hierarchical porous In_2S_3@CNT/SS cathode towards a flexible Li-CO_2 battery. *Angew. Chem., Int. Ed.* **2020**, *59*, 19518–19524.

[45] Li, M. L.; Wang, X. X.; Li, F.; Zheng, L. J.; Xu, J. J.; Yu, J. H. A bifunctional photo-assisted Li-O_2 battery based on a hierarchical heterostructured cathode. *Adv. Mater.* **2020**, *32*, 1907098.

[46] Wang, H. F.; Wang, X. X; Li, M. L.; Zheng, L. J.; Guan, D. H.; Huang, X. L.; Xu, J. J.; Yu, J. H. Porous materials applied in nonaqueous Li-O_2 batteries: Status and perspectives. *Adv. Mater.* **2020**, *32*, 2002559.

[47] Song, L. N.; Zhang, W.; Wang, Y.; Ge, X.; Zou, L. C.; Wang, H. F.; Wang, X. X.; Liu, Q. C.; Li, F.; Xu, J. J. Tuning lithium-peroxide formation and decomposition routes with single-atom catalysts for lithium-oxygen batteries. *Nat. Commun.* **2020**, *11*, 2191.

[48] Liu, X. M.; Zhao, L. L.; Xu, H. R.; Huang, Q. S.; Wang, Y. Q.; Hou, C. X.; Hou, Y. Y.; Wang, J.; Dang, F.; Zhang, J. T. Tunable cationic vacancies of cobalt oxides for efficient electrocatalysis in Li-O_2 batteries. *Adv. Energy Mater.* **2020**, *10*, 2001415.

[49] Allen, C. J.; Mukerjee, S.; Plichta, E. J.; Hendrickson, M. A.; Abraham, K. M. Oxygen electrode rechargeability in an ionic liquid for the Li-air battery. *J. Phys. Chem. Lett.* **2011**, *2*, 2420–2424.

[50] Lu, Y. C.; Gasteiger, H. A.; Shao-Horn, Y. Method development to evaluate the oxygen reduction activity of high-surface-area catalysts for Li-air batteries. *Electrochem. Solid-State Lett.* **2011**, *14*, A70–A74.

[51] Luo, X. Y.; Amine, R.; Lau, K. C.; Lu, J.; Zhan, C.; Curtiss, L. A.; Hallaj, S. A.; Chaplin, B. P.; Amine, K. Mass and charge transport relevant to the formation of toroidal lithium peroxide nanoparticles in an aprotic lithium-oxygen battery: An experimental and theoretical modeling study. *Nano Res.* **2017**, *10*, 4327–4336.

[52] Li, J. L.; Zhao, H. M.; Qi, H. C.; Sun, X. M.; Song, X. Y.; Guo, Z. Y.; Tamirat, A. G.; Liu, J.; Wang, L.; Feng, S. H. Drawing a pencil-trace cathode for a high-performance polymer-based Li-CO_2 battery

with redox mediator. *Adv. Funct. Mater.* **2019**, *29*, 1806863.
[53] Xu, J. J.; Wang, Z. L.; Xu, D.; Zhang, L. L.; Zhang, X. B. Tailoring deposition and morphology of discharge products towards high-rate and long-life lithium-oxygen batteries. *Nat. Commun.* **2013**, *4*, 2438.
[54] Sun, B.; Huang, X. D.; Chen, S. Q.; Munroe, P.; Wang, G. X. Porous graphene nanoarchitectures: An efficient catalyst for low charge-overpotential, long life, and high capacity lithium-oxygen batteries. *Nano Lett.* **2014**, *14*, 3145–3152.
[55] Shi, L.; Li, Z.; Li, Y. P.; Wang, G.; Wu, M. F.; Wen, Z. Y. Suppressing redox shuttle with MXene-modified separators for Li-O_2 batteries. *ACS Appl. Mater. Interfaces* **2021**, *13*, 30766–30775.